Key of Suppressed Triplet Nonradiative Transition-Dependent Chemical Backbone for Spatial Self-Tunable Afterglow

Indranil Bhattacharjee, Kikuya Hayashi, and Shuzo Hirata*

Cite This: JACS Au 2021, 1, 945–954

Read Online

ACCESS | Metrics & More | Article Recommendations | Supporting Information

ABSTRACT: Highly efficient persistent (lifetime > 0.1 s) room-temperature phosphorescence (pRTP) chromophores are important for futuristic high-resolution afterglow imaging for state-of-the-art security, analytical, and bioimaging applications. Suppression of the radiationless transition from the lowest triplet excited state (T_1) of the chromophores is a critical factor to access the high RTP yield and RTP lifetime for desirable pRTP. Logical explanations for factor suppression based on chemical structures have not been reported. Here we clarify a strategy to reduce the radiationless transition from T_1 based on chemical backbones and yield a simultaneous high RTP yield and high RTP lifetime. Yellow phosphorescence chromophores that contain a coronene backbone were synthesized and compared with yellow phosphorescent naphthalene. One of the designed coronene derivatives reached a RTP yield of 35%, which is the best value for chromophores with a RTP lifetime of 2 s. The optically measured rate constant of a radiationless transition from T_1

Conjugated core relating T_1-S_0 transition

was correlated precisely with a multiplication of vibrational spin−orbit coupling (SOC) at a T_1 geometry and with the Franck−Condon chromophore factor. The agreement between the experimental and theoretical results confirmed that the extended two-dimensional fused structure in the coronene backbone contributes to a decrease in vibrational SOC and Franck−Condon factor between T_1 and the ground state to decrease the radiationless transition. A resolution-tunable afterglow that depends on excitation intensity for anticounterfeit technology was demonstrated, and the resultant chromophores with a high RTP yield and high RTP lifetime were ideal for largely changing the resolution using weak excitation light.

KEYWORDS: persistent room temperature phosphorescence, vibrational spin−orbit-coupling, Frank−Condon factor, high-order excited state, emission microscopy
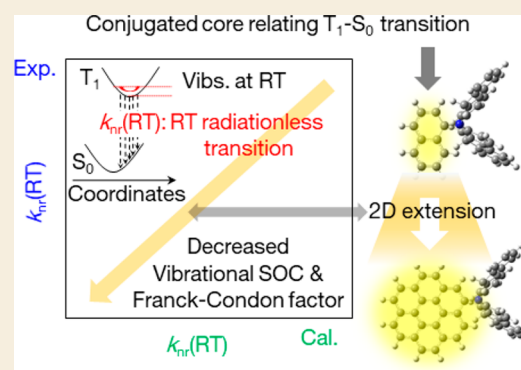
INTRODUCTION

Research interest in the field of room-temperature phosphorescence (RTP) has increased significantly in the past decade because of the versatile application of RTP in the fields of lighting,[1−3] display technology,[4−7] and bioimaging.[8,9] RTP materials with a phosphorescence lifetime at room temperature (RT) of more than 100 ms are termed persistent RTP (pRTP). pRTP materials can detect emissions after excitation ceases by using small-scale and low-cost photodetectors with a slow response time and that are independent of fluorescence from impurities.[10−13] These characteristics allow for high-contrast contactless imaging for state-of-the-art security[14−16] and bioimaging applications.[8,17,18] From a materials perspective, such advantages can be achieved by using cost-effective long-persistent emitting particles that have been commercialized for a long time.[19−22] A futuristic application for pRTP materials is that long-persistent luminescence emitters have not achieved high-resolution afterglow imaging because they are more suitable for achieving an afterglow brightness.[12] To obtain a desirable pRTP, the enhancement of phosphorescence yield at

RT [$\Phi_p(RT)$] and the phosphorescence lifetime at RT [$\tau_p(RT)$] are critical for the materials.

$\Phi_p(RT)$ and $\tau_p(RT)$ are controlled mainly by several physical parameters: the yield of an intersystem crossing (ISC) from the lowest singlet excited state (S_1) to triplet states at RT [$\Phi_{isc}(RT)$], the radiative rate constant of phosphorescence (k_p), the rate constant of intramolecular vibration-based nonradiative transition from the lowest triplet excited state (T_1) to the ground state (S_0) at RT [$k_{nr}(RT)$], and the quenching rate of T_1 that is triggered by intermolecular processes at RT [$k_q(RT)$]. k_p acceleration with a minimization of $k_{nr}(RT)$ and $k_q(RT)$ is critical to achieve a higher $\Phi_p(RT)$. Strong triplet confinement is required to minimize $k_q(RT)$.[11,23] Long conjugated substituents that are related to the high-order
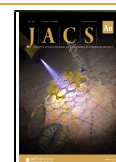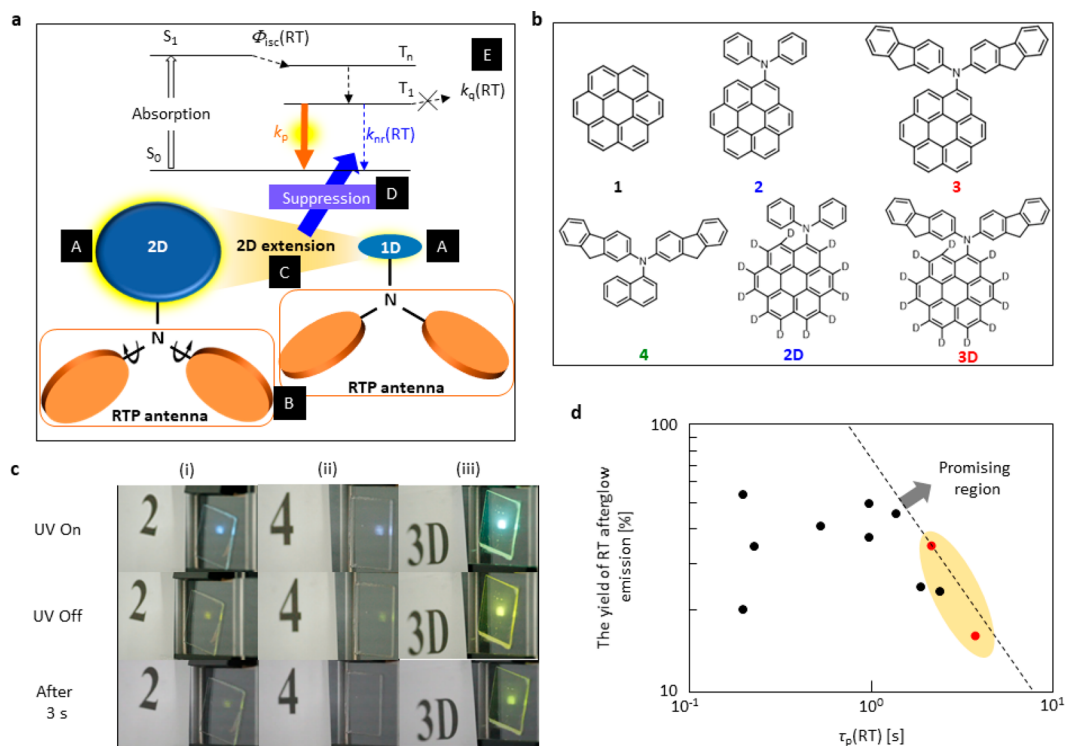
Figure 1. Molecular design, chemical structure and efficient *p*RTP. (a) Molecular design of the dopant chromophores for large $\Phi_p(RT)$ and $\tau_p(RT)$. (b) Chemical structures of the chromophores used in this study. (c) Photographs of **2** (i), **4** (ii), and **3D** (iii) under (top), soon after ceasing (middle), and 3 s after ceasing (bottom) the UV excitation at 360 nm (3.94 mW cm^{-2}) when the white room light intensity was 0.05 mW cm^{-2}. (d) Relationship between $\Phi_p(RT)$ and $\tau_p(RT)$ of the reported chromophores and chromophores studied in this report. Red dots in the shaded area indicate the chromophores in this report, and black dots are the reported chromophores.

singlet state (S_n) enhance k_p,[12] and rigid amorphous host materials with a higher T_1 energy level can be used to suppress $k_q(RT)$.[11] For $k_{nr}(RT)$, a decrease by using the isotope effect has been reported.[11] However, no clear strategy exists to reduce $k_{nr}(RT)$ as a function of chemical structure beyond the isotope effect.

We provide an effective design strategy for heavy-atom free chromophores with an efficient *p*RTP emission by decreasing $k_{nr}(RT)$ based on a conjugated backbone. Yellow phosphorescent polycyclic aromatic carbons (PACs) that were substituted with a secondary amino long conjugation were synthesized. One of the synthesized chromophores had a $\Phi_p(RT)$ of 35% with a $\tau_p(RT)$ = 2.2 s when deuterated and used in an appropriate host. A two-dimensional fused extension of the PACs with long conjugated substituents accelerated k_p and suppressed $k_{nr}(RT)$, which led to a simultaneous large $\Phi_p(RT)$ and large $\tau_p(RT)$. The optically measured $k_{nr}(RT)$ correlated well with the multiplication of vibrational spin−orbit coupling (SOC) at RT and the Franck−Condon factor between T_1 and S_0. Analyses of the correlation clarified that the two-dimensional fused extension of PACs decreases the vibrational SOC at RT and the Franck−Condon factor that suppresses the $k_{nr}(RT)$ for an efficient and extended RTP. Self-spatial modulation of the high-resolution afterglow depends on the excitation intensity, which allows for advanced state-of-the-art anticounterfeiting, and was demonstrated by using the chromophore. Chromophores with a large $\Phi_p(RT)$ and large $\tau_p(RT)$ were found to be suitable for largely changing the resolution using weak excitation.

RESULTS AND DISCUSSION

Design Strategy and Molecular Structures

An effective chromophore design is one of the most important prerequisites to extract the maximum efficiency from the chromophores. Our designed strategy was based on two main elements: PAC determines the *p*RTP emission color, which is termed the RTP center (A in Figure 1a), and the twisted long π-conjugated secondary amine substituent is termed the RTP antenna (B in Figure 1a). The effect of the RTP antenna to enhance $\Phi_{isc}(RT)$ and k_p has been discussed in our previous report.[12,24] In this work, we show that a two-dimensional delocalization of the RTP center (C in Figure 1a), substituted with the RTP antenna, decreased $k_{nr}(RT)$ (D in Figure 1a) for a simultaneous large $\Phi_p(RT)$ and $\tau_p(RT)$.

We used coronene as the RTP center and substituted a secondary amine to determine the effect of this substitution. In Figure 1b, **1−3** were used to establish the role of substitution on the RTP center and the effect of the extended conjugation length of the RTP antenna. **4** (Figure 1b) was used to monitor the effect of the RTP center, which changed to naphthalene to keep the RTP antenna the same as **3**, on the photophysical parameters between **3** and **4**. The chromophores were prepared by the method in the Supporting Information (see section S1 and Figures S1−S6).

Optical Properties

We used **2**, **4**, and **3D** as dopant chromophores to demonstrate the *p*RTP efficiency in bright room light. The emission intensities in bright room light (power density 0.05 mW cm^{-2}) are shown in Figure 1c. β-Estradiol was used as a host for all chromophores (0.3 wt %) to suppress $k_q(RT)$, as the host has a
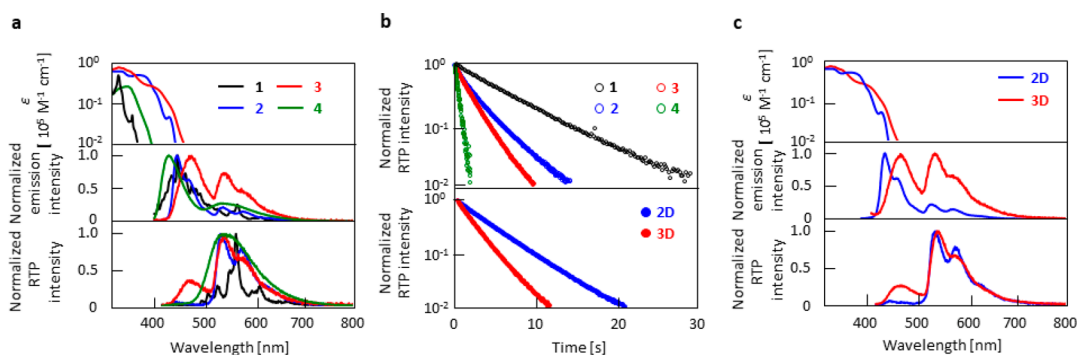
Figure 2. Optical properties. (a) Absorption spectra (top graph), emission spectra under excitation (middle graph), and emission spectra soon after ceasing excitation (bottom graph) of 0.3 wt % **1−4** doped in amorphous β-estradiol. (b) RTP decay characteristics of 0.3 wt % **1−4** doped in amorphous β-estradiol (top graph) and 0.3 wt % **2D** and **3D** doped in amorphous β-estradiol (bottom graph). (c) Absorption spectra (top graph), emission spectra under excitation (middle graph), and emission spectra soon after ceasing excitation (bottom graph) of 0.3 wt % **2D** and **3D** doped in amorphous β-estradiol.

Table 1. Photophysical Parameters of 1−4, 2D, and 3D Related to Fluorescence and ISC from S_1

chromophore	$\Phi_f(RT)$ [%][a]	$\tau_f(RT)$ [10^{-9} s][a]	k_f [10^7 s^{-1}][b]	λ_f [nm][c]	$\Phi_{isc}(RT)$ [%][d]	$k_{isc}(RT)$ [10^7 s^{-1}][g]
1	25	238	0.1	445	$(42 \pm 11^{f)})^e$	0.2
2	24	17.3	1.4	445	76 $(88 \pm 22)^e$	4.4
3	20	7.03	2.8	472	80 $(84 \pm 21)^e$	11
4	22	2.78	8.1	425	78 $(89 \pm 22^f)^e$	28
2D	26	18.3	1.4	445	74 $(82 \pm 21)^e$	4.1
3D	19	7.14	2.7	472	81$(86 \pm 22)^e$	11

[a]Values using 0.3 wt % chromophore doped in β-estradiol. [b]Calculated $k_f = \Phi_f(RT)/\tau_f(RT)$. [c]Peak wavelength of fluorescence. [d]$\Phi_{isc}(RT) = 1 - \Phi_f(RT)$, and parentheses indicate values measured using transient absorption method in ref 32. [e]The data of $\Phi_{isc}(RT)$ by transient absorption generally has errors of ±25% of the values as reported in ref 33. [f]Values reported in Table 1 in ref 24. [g]$k_{isc}(RT) = \Phi_{isc}(RT)/\tau_f(RT)$.

higher T_1 energy level and intrinsic rigid nature (E in Figure 1a).[11,12,24] The doped materials were sandwiched in the amorphous state between two glass substrates, and the film absorbance at 360 nm was 0.40. When the films were excited using ultraviolet (UV) light at 360 nm (power density 3.94 mW cm^{-2}), chromophores **2** and **4** showed similar emission intensities during the UV excitation, whereas **3D** showed a brighter emission compared with that of the earlier two (top photos of (i)−(iii) in Figure 1c). Immediately after ceasing the UV excitation, a yellow *p*RTP emission was detected for **2** and **4** (middle photos of (i) and (ii) in Figure 1c), but a bright-yellow *p*RTP emission from **3D** was detected easily by the naked eye (middle photo of (iii) in Figure 1c) under bright-white room light. The existence of a yellow *p*RTP emission of **2** and **4** disappeared rapidly within a few seconds because of the low brightness and longevity of the *p*RTP emission (bottom photos of (i) and (ii) in Figure 1c), and for **3D** the yellow *p*RTP emission remained (bottom photo of (iii) in Figure 1c and Movies S1−S3). Because the sample absorbance was the same at 360 nm (Figure S7), the difference in *p*RTP brightness and endurance occurred only because of the large difference in $\Phi_p(RT)$ and $\tau_p(RT)$. In Figure 1d, to the best of our knowledge, we have shown that the reported chromophores had a $\Phi_p(RT) \geq 20\%$ with $\tau_p(RT) \geq 0.1$ s.[12,25−30] This example fulfills the given criteria, even though a combination of $\Phi_p(RT) \geq 20\%$ with $\tau_p(RT) \geq 1.0$ s shortens the window. In this work, we have shown that the chromophores have a $\tau_p(RT)$ greater than 2 s with a $\Phi_p(RT)$ of 35%, which is at the highest level for $\Phi_p(RT)$ and $\tau_p(RT)$. A $\Phi_p(RT)$ of 35% is the highest for materials with $\tau_p(RT) \geq 2$ s.

Chromophores **1−4** (0.3 wt %) in the amorphous β-estradiol show a large, structured absorption band below 400

nm, which can be assigned to a $\pi-\pi^*$ transition. A broad absorption band was visible at ∼380−440 nm for **2−4** because of charge transfer (CT) from the RTP antenna to the RTP center (top graph of Figure 2a). Chromophores **1−4** showed emission spectra from 410 to 750 nm under UV-light excitation (middle graph of Figure 2a). The origin of the emission peak from 410 to 500 nm resulted because of the fluorescence, as the lifetime of these emissions was in the nanosecond range (Figure S8). The fluorescence quantum yields at RT ($\Phi_f(RT)$), fluorescence lifetimes ($\tau_f(RT)$), rate constant of fluorescence (k_f), quantum yield of the intersystem crossing from S_1 to the triplet states at RT ($\Phi_{isc}(RT)$), and the rate constant of intersystem crossing from S_1 to the triplet states at RT ($k_{isc}(RT)$) of the 0.3 wt % doped **1−4** in β-estradiol are summarized in Table 1 (Figures S9−S11 and Table S1). For **1**, the small k_f can be explained by a symmetric forbidden transition (Figure S12).[31] For **2−4**, the enhancement of k_f was observed because the allowed CT transition nature appears with fluorescence by an introduction of the RTP antenna (Figure S12). Introduction of the RTP antenna enhanced k_f and increased $k_{isc}(RT)$, as also observed in the calculations (see section S3 and Figures S13−S16). A comparison of the extent of enhancement between k_f and $k_{isc}(RT)$ shows that the increase in $k_{isc}(RT)$ dominates and results in a large $\Phi_{isc}(RT)$ for **2−4** (Table 1).

After ceasing the excitation, chromophores **1−4** show emission spectra from ∼500 to 750 nm for a few seconds (bottom graph of Figure 2a). The decay characteristics approach a single-exponential decay of this persistent emission (top graph of Figure 2b), which indicates that this emission results because of the *p*RTP characteristics of the chromophores. The $\tau_p(RT)$ of 0.3 wt % doped **1−4** in β-estradiol was

Table 2. Photophysical Parameters of 1−4, 2D, and 3D Related to pRTP

chromophore	$\Phi_p(RT)$ [%][a]	$\tau_p(RT)$ [10° s][a]	λ_p [nm][b]	k_p [s^{-1}][c]	$k_{nr}(RT)$ [s^{-1}][d]	$k_q(RT)$ [s^{-1}][e]
1	3.4	6.0	567	0.01	0.12	0.04
2	11	3.1	540	0.05	0.23	0.04
3	19 (4)[f]	1.8 (1.1)[f]	545	0.13	0.27	0.15
4	10	0.45	550	0.30	1.8	0.12
2D	16	3.8	540	0.06	0.16	0.05
3D	35 (6)[f]	2.2 (1.4)[f]	545	0.20	0.16	0.10

[a]Values using 0.3 wt % chromophore doped in β-estradiol. [b]Peak wavelength of phosphorescence. [c]Values determined by substituting experimentally observed $\Phi_p(RT)$, $\tau_p(RT)$, and $\Phi_{isc}(RT) = 1 - \Phi_f(RT)$ into $k_p = \Phi_p(RT)\Phi_{isc}(RT)^{-1}\tau_p(RT)^{-1}$. [d]Values determined using fitting lines of $k_{nr}(T)$. [e]Values determined by subtracting $k_{nr}(RT)$, which is determined using the fitting lines of $k_{nr}(T)$, from experimentally observed $k_{nr}(T) + k_q(T)$. [f]Parentheses indicates TADF values.

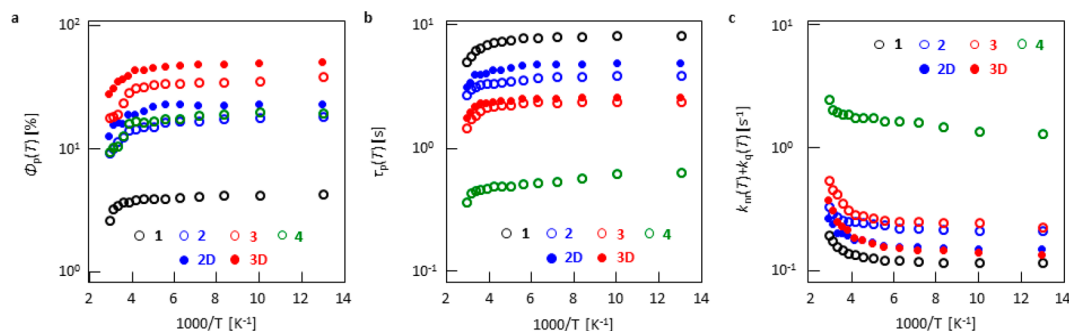**Figure 3.** Temperature-dependent analysis of **1−4**, **2D**, and **3D**. (a) $\Phi_p(T)$, (b) $\tau_p(T)$, and (c) $k_{nr}(T) + k_q(T)$. $\Phi_p(T)$ and $\tau_p(T)$ were measured under vacuum conditions, whereas $\Phi_p(RT)$ and $\tau_p(RT)$ did not show any change between vacuum and ambient conditions.

6.0, 3.1, 1.8, and 0.45 s, respectively (top graph of Figure 2b, Table 2). $\Phi_p(RT)$ of 0.3 wt % doped **1−4** in β-estradiol was separated by using time-dependent emission spectral analysis (see section S4 and Figure S17) and quantified as 3.4%, 11%, 19%, and 10%, respectively (Table 2). Comparable excitation spectra of pRTP with absorption spectra indicate that the observed pRTP was not caused by impurities (Figure S18). In **3**, the afterglow RT emission yield was 23%, which included the contribution of afterglow thermally activated delayed fluorescence (TADF) (Table 2). The afterglow RT emission yield above 20% is the top level of molecular solids with an afterglow lifetime of approximately 2 s.[25,29,34] Because the large $\Phi_p(RT)$ and $\tau_p(RT)$ are based on a chemical backbone of **3**, clarification of more logical points that led to the result is useful for the design of chromophores with larger $\Phi_p(RT)$ and longer $\tau_p(RT)$. Deuteration of **2** and **3** was performed to improve $\Phi_p(RT)$ and $\tau_p(RT)$. Chromophores **2D** and **3D** showed identical absorption spectra compared with that of **2** and **3** (top graph of Figure 2c). In the steady-state emission spectra, a significant enhancement of yellow pRTP emission occurred (middle graph of Figure 2c), with a similar pRTP emission spectral shape compared with that of **2** and **3** (bottom graph of Figure 2c). An enhancement of $\tau_p(RT)$ was also observed (bottom graph of Figure 2b). Although $\Phi_f(RT)$ and $\tau_f(RT)$ of **2D** and **3D** hardly changed compared with undeuterated chromophores (Table 1), $\Phi_p(RT)$ of **2D** and **3D** was 16% and 35%, respectively, whereas the $\tau_p(RT)$ of **2D** and **3D** was 3.8 and 2.2 s, respectively, when doped into β-estradiol (Table 2). **3D** in β-estradiol presented an afterglow TADF with a 6% yield and a lifetime of 1.4 s (Table 2) because the spectral signal could be observed soon after excitation (bottom of Figure 2c). Therefore, an afterglow RT emission yield of **3D** reached 41%. Because **2D** and **3D** had a comparable $\Phi_{isc}(RT)$ to that of **2** and **3** (Table 1), respectively, the enhancement of $\Phi_p(RT)$ and $\tau_p(RT)$ resulted mainly because the suppression

of $k_{nr}(RT)$ was caused by a general isotope effect (Table 2).[11,12,35−37] Although an increase in the $\tau_p(RT)$ from the decrease in $k_{nr}(RT)$ by the isotope effect has been reported, $\Phi_p(RT)$ was often 10%−20% for chromophores with a $\tau_p(RT)$ greater than 2 s.[11] However, this combination of isotope effect and decrease in $k_{nr}(RT)$ owing to the appropriate chemical backbone increased $\Phi_p(RT)$ to 35%.

Temperature-Dependent Analysis

Because the effect of deuteration to suppress the $k_{nr}(RT)$ between **2** and **2D** or **3** and **3D** is a well-known and established science,[11,12,35−37] we considered the reason for the significant difference in photophysical properties depending on the chemical structures of **1−4**. To assess the reason for this behavior, we need to establish the related physical parameters. $\Phi_p(RT)$ and $\tau_p(RT)$ are generally expressed as[11,23]

$$\Phi_p(RT) = \Phi_{isc}(RT)k_p\tau_p(RT) \tag{1}$$

$$\tau_p(RT) = 1/(k_p + k_{nr}(RT) + k_q(RT)) \tag{2}$$

Equations 1 and 2 indicate that a large $\Phi_{isc}(RT)$, large k_p, and small $k_{nr}(RT) + k_q(RT)$ are essential for the large $\Phi_p(RT)$ and $\tau_p(RT)$. Because $\Phi_{isc}(RT)$ was comparable and large for **2−4**, the different $\Phi_p(RT)$ was caused by the difference of k_p, $k_{nr}(RT)$, and $k_q(RT)$. To investigate these three factors, first we estimated k_p of **1−4** by substituting $\Phi_{isc}(RT)$, $\Phi_p(RT)$, and $\tau_p(RT)$ into eq 1 (Table 1). Next, a temperature-dependent analysis of $\Phi_p(T)$ and $\tau_p(T)$ was performed to establish the $k_{nr}(RT)$ and $k_q(RT)$ of **1−4**. The temperature-dependent analysis shows that $\Phi_p(T)$ decreased slightly from 77 K to RT (Figures 3a and S19) and a similar tendency was also observed for the $\tau_p(T)$ for all chromophores (Figures 3b and S20). A substitution of k_p and the dependence of $\tau_p(T)$ into eq 2 yielded the temperature-dependent $k_{nr}(T) + k_q(T)$ (Figure 3c). The plot could be fitted into a sum of two exponential

Table 3. Calculated Photophysical Parameters Related to Triplet States of 1−4

chromophore	$\langle T_1|\hat{H}_{SO}|S_0\rangle^2$ [cm^{-2}][a]	Σ_PVSOC(RT)FC [au][a]	Σ_PVSOC(RT) [au][a]	η	$(E_{T_1-S_0} - E_0)/\eta$ [10^3 cm^{-1}][b]	FC [10^{-5} au][c]
1	3.4×10^{-7}	4.7×10^{-5}	5.8×10^{0}	0.333	40.9	0.81
2	4.2×10^{0}	9.9×10^{-5}	8.7×10^{0}	0.368	39.4	1.14
3	3.9×10^{-1}	1.2×10^{-4}	1.0×10^{1}	0.367	39.1	1.23
4	6.3×10^{-1}	5.9×10^{-4}	1.7×10^{1}	0.410	34.6	3.42

[a]Calculated values using the PBE0 functional and TZP basis sets using optimized structure at T$_1$ by DFT (Gaussian09/B3LYP/6-31G(d)). [b]Data of λ_p in Table 2 used to determine $E_{T_1-S_0}$. [c]Data determined by substituting $(E_{T_1-S_0} - E_0)/\eta$ into log FC $\approx [10^{-4}(E_{T_1-S_0} - E_0)/\eta]^{-1} - 1$, which is summarized in Figure 7 in ref 36.

equations (Figure S21). In a previous report, it was confirmed that a large increase of $k_{nr}(T) + k_q(T)$ in a higher-temperature region is caused by $k_q(T)$[11,38] and the lower temperature component is caused by $k_{nr}(T)$, which depends on the vibrational SOC and Franck−Condon factor between T$_1$ and S$_0$ of the chromophores.[24,39]

After the temperature-dependent estimation of $k_{nr}(T)$ of 1−4, the estimated values of $k_{nr}(RT)$ for 1−4 were 1.2×10^{-1}, 2.3×10^{-1}, 2.7×10^{-1}, and 1.8×10^{0} s^{-1}, respectively. The quantified k_p and $k_{nr}(RT)$ of 1−4 are summarized in Table 2.

An incorporation of the substituent (comparison of 1 and 2) to coronene, which acted as a RTP center, was responsible for the enhancement of k_p and $k_{nr}(RT)$. Because the enhancement of k_p was larger than that of $k_{nr}(RT)$, the substituents led to an increase of $\Phi_p(RT)$ from 3.4% for 1 to 11% for 2. A similar tendency was observed, depending on the change from 2 to 3 when the conjugation length of the RTP antenna increased. The enhancement of k_p was greater compared with that of $k_{nr}(RT)$. As a result, $\Phi_p(RT)$ increased from 11% for 2 to 19% for 3. We have already reported that the enhancement of k_p using RTP antenna can be explained by the increase of the S$_n$−S$_0$ transition dipole moment caused by an extension of the RTP antenna.[12] The tendency was observed as well in the comparison between 1−3 (see section S5 and Figure S22). However, a different tendency with the increase of k_p being much less than that of $k_{nr}(RT)$ was observed when the RTP center changed from the coronene for 3 to the naphthalene for 4.

Effect of RTP Center for $k_{nr}(RT)$ Suppression

The origin of the suppression of $k_{nr}(RT)$ of 3 compared with that of 4 needs to be understood for a comprehensive molecular level understanding. Without any consideration of molecular coordination change that is caused by vibrations, $k_{nr}(RT)$ is often expressed based on a nonadiabatic SOC between T$_1$ and S$_0$ ($\langle T_l|\hat{H}_{SO}|S_0\rangle$) as[40]

$$k_{nr} = \frac{2\pi}{\hbar}|\langle T_l|\hat{H}_{SO}|S_0\rangle|^2 FC \tag{3}$$

where FC is the Frank−Condon factor. The calculated $\langle T_l|\hat{H}_{SO}|S_0\rangle^2$ for 1−4 were 3.4×10^{-7}, 4.2×10^{0}, 3.9×10^{-1}, and 6.3×10^{-1} cm^{-2}, respectively (Table 3). A poor correlation resulted when these values were plotted against the experimental $k_{nr}(RT)$ (Figure 4a). We have reported a calculation method to predict $k_{nr}(RT)$ of a variety of undeuterated chromophores with free vibrations allowed by energy corresponding room-temperature.[24] The calculation was based on an approximation that $k_{nr}(RT)$ is an approximate multiplication of the vibrational SOC term of the equation that considers the Herzberg−Teller SOC and FC. In theory, $k_{nr}(RT)$ is approximately expressed as
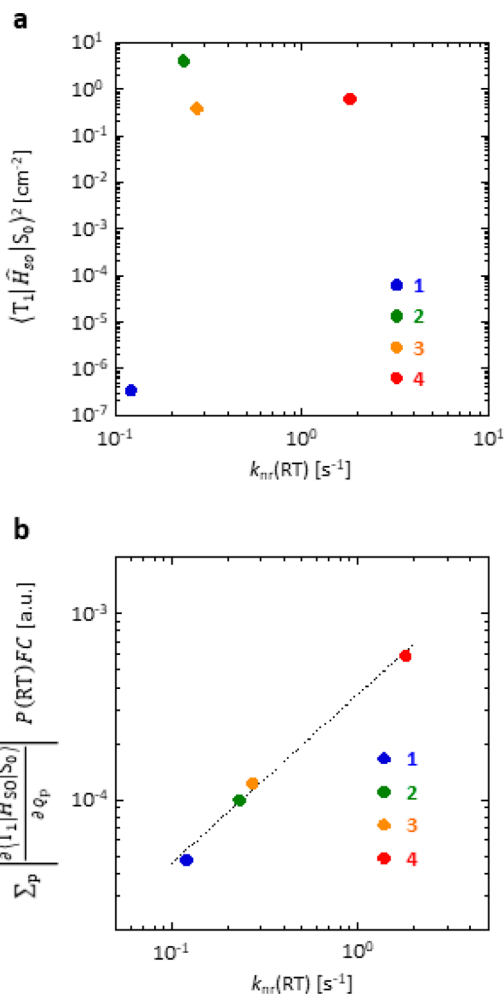
Figure 4. Relationship between $k_{nr}(RT)$ and nonadiabatic SOC and SOC considering vibrations allowed at RT. (a) Relationship between $\langle T_l|\hat{H}_{SO}|S_0\rangle^2$ and $k_{nr}(RT)$ for 1−4. (b) Relationship between $\sum_p|\partial\langle T_l|\hat{H}_{SO}|S_0\rangle/\partial Q_p|^2 P(RT)$ and $k_{nr}(RT)$ for 1−4. The slope of the dashed fitting line based on the least-squares method is 0.91.

$$k_{nr}(RT) \propto 2\pi \sum_P \left|\partial\langle T_l|\hat{H}_{SO}|S_0\rangle/\partial Q_p\right|^2 P(RT)FC \tag{4}$$

where Q_P is the mass-weighted normal coordinate that corresponds to the pth vibrational mode at T$_1$ and $P(RT)$ is the vibrational factor at RT. The calculated $\sum_p|\partial\langle T_l|\hat{H}_{SO}|S_0\rangle/\partial Q_p|^2 P(RT)FC$ for 1−4 are 4.7×10^{-5}, 9.9×10^{-5}, 1.2×10^{-4}, and 5.9×10^{-4} au, respectively (Table 3). This result has an excellent correlation with the optically measured $k_{nr}(RT)$ (Figure 4b) and a strong correlation was
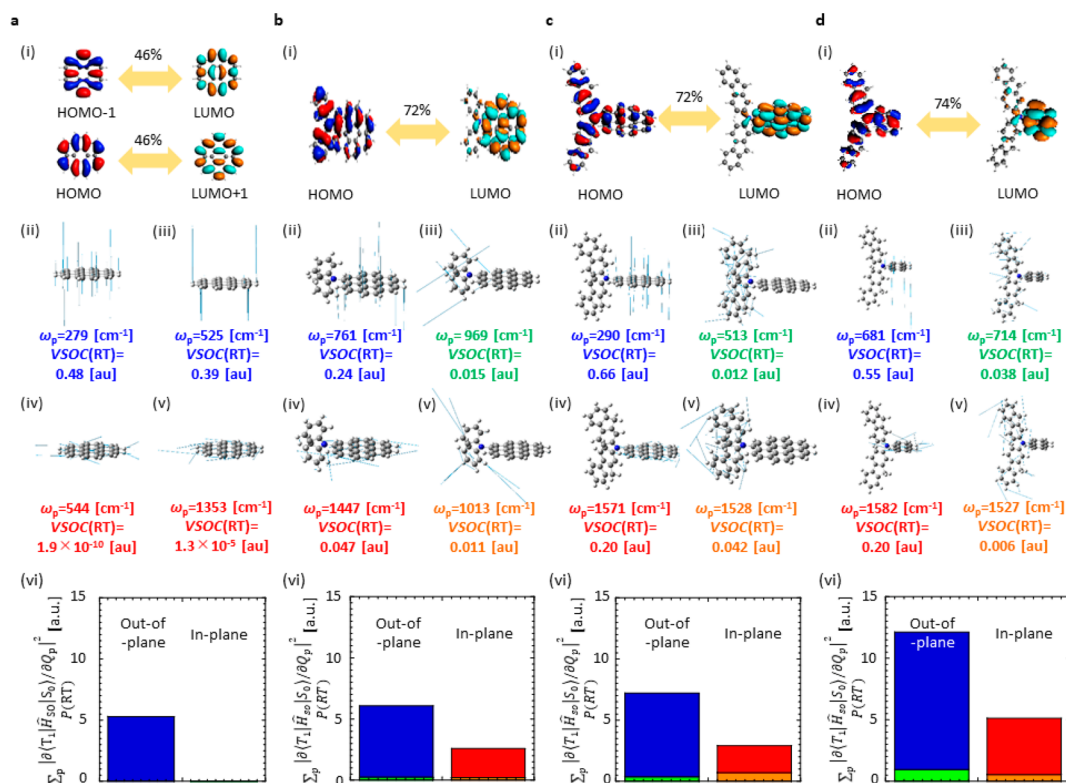
Figure 5. Nature of transition and analysis of $k_{nr}(RT)$ depending on VSOC(RT) of **1−4**. (a) **1**, (b) **2**, (c) **3**, and (d) **4**. In (a)−(d), the mode of transition at the T_1 geometry (i), VSOC(RT) in the representative vibration modes (ii)−(v), total magnitude of VSOC(RT) considering all possible out-of-plane vibration modes of RTP center (blue shaded are), all possible in-plane vibration modes of RTP center (red shaded area), all possible out-of-plane vibration modes of RTP antenna (green shaded area), and all possible in-plane vibration modes of RTP antenna (orange shaded area) (vi).

observed in a variety of chromophores with different RTP colors (Figures S23, S24 and Table S2−S7). Therefore, the correlation allows for a deeper analysis of the relationship between $k_{nr}(RT)$ and the molecular structure. Because eq 4 is constructed mainly from two factors; $\sum_p |\partial\langle T_1|\hat{H}_{SO}|S_0\rangle/\partial Q_p|^2 P(RT)$, where $|\partial\langle T_1|\hat{H}_{SO}|S_0\rangle/\partial Q_p|^2 P(RT)$ is abbreviated as VSOC(RT) for easier reading, and FC, we first analyzed $\sum_p$VSOC(RT) of **1−4** in the following paragraph.

The difference of $\sum_p$VSOC(RT) among **1−3** is explained depending on the different nature of the $T_1−S_0$ transition, whereas that between **3** and **4** was caused by the different sizes of fused rings of the RTP center. For **1−3** as chromophores with coronene as a RTP center, $\sum_p$VSOC(RT) increased slightly by introducing RTP antennas as substituents and an extension of the antenna. For **1**, out-of-plane modes of coronene (RTP center) were predominantly responsible for the $k_{nr}(RT)$ and the overall VSOC(RT) was 5.8×10^0 au. (Table 3). Because $\langle T_1|\hat{H}_{SO}|S_0\rangle$ differs depending on the out-of-plane vibrations, the out-of-plane vibrations have a large VSOC(RT) ((ii) and (iii) in Figure 5a). Because $\langle T_1|\hat{H}_{SO}|S_0\rangle$ hardly changes depending on the in-plane vibrations, the in-plane vibrations have a small VSOC(RT) ((iv) and (v) in Figure 5a). The tendency was confirmed by checking that the integration of VSOC(RT) for all out-of-plane vibrations (blue shaded area in (vi) of Figure 5a) was larger than that of the in-plane vibrations (red shaded area in (vi) of Figure 5a). For **2** and **3**, however, the in-plane vibrations of the coronene moiety

((iv) in Figure 5b and c) and the out-of-plane vibrations of the coronene unit ((ii) of Figure 5b and c) enhanced the $k_{nr}(RT)$ (blue and red shaded area in (vi) of Figure 5b and c). The overlapping density of the two molecular orbitals (MOs) is related to the $T_1−S_0$ transition located at the coronene part and at the slightly conjugated substituents ((i) in Figure 5b and c). Because the in-plane vibrations of coronene were not parallel to the conjugated plane of the conjugated substituents, the vibrations allow for spin flipping for the electron at the substituents. Therefore, in- and out-of-plane vibrations of the coronene part contribute to an increase in $\sum_p$VSOC(RT). However, vibrations of the substituents hardly increase $\sum_p$VSOC(RT) (green and orange shaded area in (vi) of Figure 5b and c). Consequently, the overall calculated values of $\sum_p$VSOC(RT) for **2** and **3** are 8.7×10^0 and 1.0×10^1 au, respectively, which increase slightly compared with that of **1** (Table 3). The slight increase from **1** to **2** and **3** may be explained by the increase in the CT nature for the $T_1−S_0$ transition. Because $\sum_p$VSOC(RT) increases largely when the $T_1−S_0$ transition has a strong CT nature, such as for benzophenone,[24] a slight increase of the CT nature that is caused by the substituents for **2** and **3** ((i) in Figure 5a) compared with **1** ((i) in Figure 5b and c) explains the increase in $\sum_p$VSOC(RT). A larger difference of $\sum_p$VSOC(RT) that is independent of the nature of the $T_1−S_0$ transition was observed between **3** and **4**. The contribution of the HOMO−LUMO transition to the $T_1−S_0$ transition is comparable between **3** ((i) in Figure 5c) and **4** ((i) in Figure 5d). However, the $\sum_p$VSOC(RT) of **4** is 1.7 times larger than that of **3** (Table 3). Compared with **3** (blue and red shaded
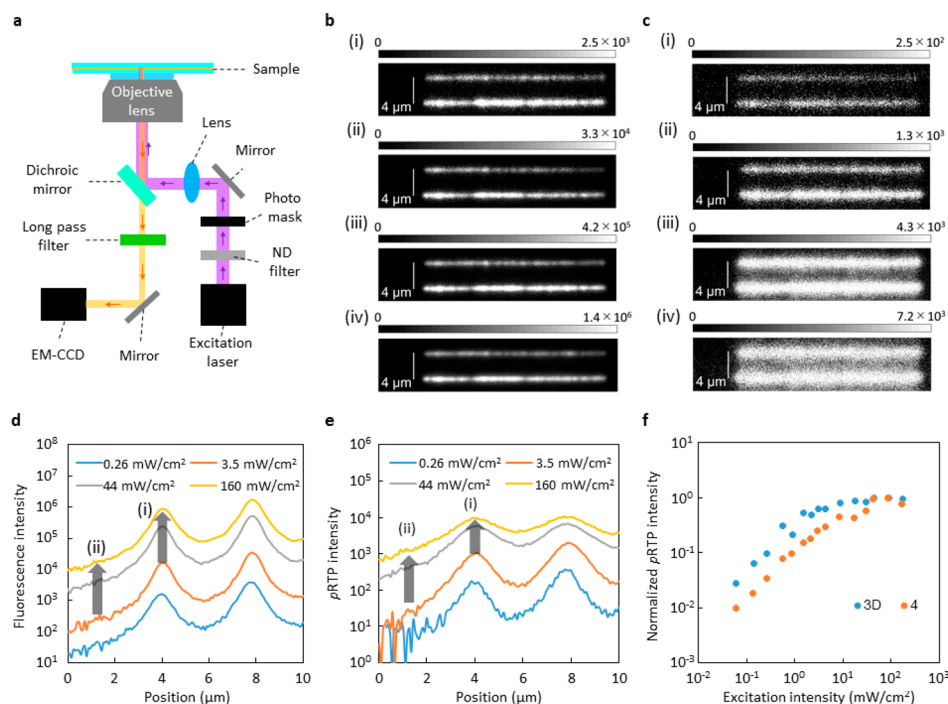
Figure 6. Self-spatial modulation of high-resolution afterglow. (a) Optical setup for demonstration. (b) Fluorescence images of sample F8BT under 445 nm excitation with difference in irradiance. (c) Afterglow images of sample 3D integrated for 0.1 s after ceasing 445 nm excitation with difference in irradiance. In (b) and (c), (i) 2.6×10^{-1} mW/cm^2, (ii) 3.5×10^{0} mW/cm^2, (iii) 4.4×10^{1} mW/cm^2, and (iv) 1.6×10^{2} mW/cm^2. (d) Intensity profiles of fluorescence line width of sample F8BT at difference excitation intensity of 445 nm. (e) Intensity profiles of persistent RTP line width of sample **3D** integrated for 0.1 s after ceasing 445 nm excitation with difference in irradiance. (f) Difference of pRTP intensity depending on excitation intensity at 355 nm for sample **3D** and sample **4**. The saturated intensity was normalized to 1.

areas in (vi) of Figure 5c), the contribution of out-of-plane and in-plane vibrations of **4** (blue and red shaded areas in (vi) of Figure 5d) to increase Σ_pVSOC(RT) is large. A comparison of **3** and **4** shows that the extension of the two-dimensional fused ring contributes to a decrease in Σ_pVSOC(RT) for smaller k_{nr}(RT).

Because FC is related to k_{nr}(RT) based on eq 4, a careful check of the contribution to k_{nr}(RT) is necessary. Although all chromophores showed a comparable yellow pRTP, which indicates a comparable energy difference between T$_1$ and S$_0$ ($E_{T_1-S_0}$) (bottom of Figure 2a and Table 2), it was noted that FC depends on $E_{T_1-S_0}$ and on the relative number of hydrogen atoms in the molecule (η), which is defined as C$_{1-\eta}$H$_\eta$.[36] As the number of nitrogen atoms in **2−4** is small compared with the total number of atoms, η of **1−4** is determined as shown in Table 3. The values of FC were determined by substituting $E_{T_1-S_0}$ and η into log FC $\approx [10^{-4}(E_{T_1-S_0} - E_0)/\eta]^{-1} - 1$, where $E_0 = 4000$ cm^{-1} is the empirical parameter by Siebrand (Figure S25).[36,41,42] The FC of **1−4** is summarized in Table 3. For **1−3**, FC is comparable, but for **4** it increases significantly (Table 3). The large decrease in FC from **4** to **3** is explained because of the decrease in η when log FC $\approx [10^{-4}(E_{T_1-S_0} - E_0)/\eta]^{-1} - 1$ is considered. The decrease in the number of hydrogen atoms compared with other atoms because a two-dimensional fused extension of the RTP center corresponds to a decrease in η and FC could be reduced by the two-dimensional fused extension of the RTP center. The overall calculation result for Σ_pVSOC(RT) and FC indicates that a two-dimensional fused extension of the RTP center tends to decrease Σ_pVSOC(RT) and FC to allow a large decrease in k_{nr}(RT) to improve Φ_p(RT) and τ_p(RT).

Self-Spatial Modulated High-Resolution Afterglow

A change in photopatterned spatial information requires a mechanical change of optics, including photomasks. If the materials automatically change emission spatial information independent of the mechanical changes, they reach a point that has not been obtained by other materials and technologies. For example, a 445 nm high-resolution light through a photomask and objective lens was irradiated on a poly[(9,9-di-*n*-octylfluorenyl-2,7-diyl)-*alt*-(benzo[2,1,3]thiadiazol-4,8-diyl)] (F8BT) film on a glass substrate (sample F8BT) and 3 wt % **3D** doped amorphous β-estradiol film between two glass substrates (sample **3D**). Figure 6a provides a schematic illustration of the high-resolution imaging technique that was used in this demonstration. For sample F8BT, two lined high-resolution yellow fluorescence patterns according to the photomask appeared under a weak excitation at 2.6×10^{-1} mW/cm^2 (Figure 6b; (i)). The line widths did not change when the excitation power density increased gradually to 1.6×10^2 mW/cm^2 (Figure 6b; (ii)−(iv)). For sample **3D**, yellow afterglow phosphorescence patterns of sample **3D** soon after ceasing the 445 nm excitation light are shown in Figure 6c. Although a similar high resolution of the afterglow lines was observed when the excitation power density was weak (2.6×10^{-1} mW/cm^2) (Figure 6c; (i)), a distinct broadening of only high-resolution lines were observed with an increase in excitation intensity to 1.6×10^2 mW/cm^2 (Figure 6c; (ii)−(iv)). A broadening of emission lines was not observed for steady-state emission under strong excitation because fluorescence without strong annihilation became extremely dominant in the strong excitation (Figure S26).

The large broadening is related largely to a saturation of pRTP intensity, which depends on excitation intensity. It has

been reported that saturation occurs because of annihilation that is caused mainly by a singlet−triplet resonance energy transfer and a triplet−triplet resonance energy transfer because of a concentrated accumulation of triplet excitons in the materials.[43,44] In epifluorescent imaging with a resolution that approaches the diffraction limit, the excitation profile of the line width does not have a top-hat shape. Therefore, the emission profile has a center ((i) in Figure 6d) and tail parts ((ii) in Figure 6d). For sample F8BT, the fluorescence intensity at the center and tail approximately increases 50 times when the excitation intensity increases from 3.5 to 160 mW/cm^2 ((i) and (ii) in Figure 6d). Therefore, the shape of the fluorescence profile is independent of the power (Figure 6d). For sample 3D, the afterglow intensity at the center part ((i) in Figure 6e) increased only 9 times, whereas that at the tail ((ii) in Figure 6e) increased approximately 50 times when the excitation intensity increased from 3.5 to 160 mW/cm^2. Because of the much larger increase in afterglow intensity at the tail part compared with that at the center, a large broadening of the afterglow emitting lines was observed with an increase in excitation intensity.

The simultaneous large $\Phi_p(RT)$ and $\tau_p(RT)$, such as those for 3D, are suitable for the self-spatial modulation of a high-resolution afterglow. To determine the extent of saturation, we measured the power-dependent pRTP intensity. Chromophore 4, 3 wt % doped in amorphous β-estradiol film between two glass substrates (sample 4), was used as a reference sample. The absorbance of samples 3D and 4 were comparable (Figure S27). Compared with sample 4, the pRTP of sample 3D was saturated in a weaker excitation intensity (Figure 6f). Because the triplet accumulation to induce the saturation depends theoretically on a multiplication of $\Phi_{isc}(RT)$ and $\tau_p(RT)$[31] and 3D and 4 have a comparable $\Phi_{isc}(RT)$ (Table 1 and Table 2), the much larger $\tau_p(RT)$ of 3D compared with 4 allows for a self-spatial modulation in weaker excitation light. A high-power light source is required for epi-emission imaging compared with confocal imaging for two-dimensional homogeneous excitation. Therefore, a decrease in excitation intensity in the light source is recommended for mobile applications. The decrease in $\Phi_p(RT)$ is not accepted when materials show a longer $\tau_p(RT)$ because the brightness of the afterglow decreases and causes no signal in the high-resolution imaging because the brightness became less than the dark noises of the two-dimensional photodetectors. Because two-dimensional photodetectors that are used in mobile applications do not tend to have cooling and a significant amplifier, a large $\Phi_p(RT)$ is required to allow for a high-resolution afterglow and to decrease the error for a readout of a high-resolution afterglow. A large $\tau_p(RT)$ is needed for the large self-spatial modulation of the high-resolution afterglow. Therefore, a chemical approach to suppress $k_{nr}(RT)$ without a large decrease in k_p for chromophores is critical to achieve materials with a large $\Phi_p(RT)$ and large $\tau_p(RT)$ and contributes to a safer advanced society. The change in the afterglow emission pattern using the waveguide mode was demonstrated.[45] However, the function may depend on the material shape, and spatial information on the low-resolution information could be obtained by using materials with different pRTP decay lifetimes in different positions. The demonstrated self-spatial tunable afterglow in this work was based on excitonic interactions that allow for a high-resolution approach to a diffraction limit level. The self-spatial tunable resolution that uses high-resolution information approaches the diffraction limit and provides a state-of-art

secret quality that previous materials and technologies have not achieved.

CONCLUSIONS

The structure−property relationship in the field of pRTP science is one of the most obvious aspects, as it provides an opportunity to improve the properties of designed chromophores. The fused two-dimensional poly aromatic carbon, coronene, acts as an RTP center, and it was substituted with a long π-conjugated RTP antenna. One of the chromophores had a $\Phi_p(RT) = 35\%$ and $\tau_p(RT) = 2.2$ s in an amorphous short conjugated rigid host at ambient conditions. A comparison of the two synthesized coronene derivatives showed that the RTP antenna enhanced k_p more than 10 times whereas the increase in $k_{nr}(RT)$ remained approximately double. A comparison of coronene and naphthalene, as the RTP center with the same RTP antenna, indicated that $k_{nr}(RT)$ decreased using a two-dimensional fused extension without a considerable decrease in k_p. For the chromophores, the optically measured $k_{nr}(RT)$ correlated precisely with a multiplication of the computationally calculated vibrational SOC and FC between T_1 and S_0. The correlation allowed for clarification that the two-dimensional fused extension decreased the vibrational SOC and FC. A guideline to the decrease in $k_{nr}(RT)$ independent of k_p is critical for large $\tau_p(RT)$ and large $\Phi_p(RT)$ from a variety of chromophores. A saturation behavior of bright pRTP characteristics owing to materials with a large $\tau_p(RT)$ and large $\Phi_p(RT)$ allowed for a tunable high-resolution afterglow depending on a weaker excitation intensity. The self-spatial modulation of a high-resolution afterglow yields difficulties for fake production, and detection using a low-cost and mobile optical setup is a promising way to increase anticounterfeit quality in secret media significantly.

EXPERIMENTAL PROCEDURES

Materials

Chromophore 1 (Tokyokasei Chemical Industries (TCI), Tokyo, Japan) and β-estradiol (TCI) are commercially available. Chromophore 1 was purified via vacuum sublimation before preparing the sample for optical measurement. Chromophores 2, 3, 2D, and 3D were synthesized and their structure was identified via ^{1}H NMR, ^{13}C NMR, high-resolution mass spectroscopy, and elementary analysis. Details are provided in the Supporting Information (see section S1). The synthesis and characterization of 4 is reported in the Supporting Information of a previous report.[12] All chromophores were used as dopant, with a 0.3% mass fraction dissolved in melted β-estradiol at 200 °C, and the mixture was spread between two quartz or glass substrates heated at 200 °C. The transparent film was obtained by gradual cooling of the substrate to RT.

Fundamental Photophysical Characteristics

Absorption spectra of all samples were measured using an absorption spectrometer (V-630, JASCO, Tokyo, Japan). The fluorescence spectra, RTP spectra, and RTP lifetime at RT were measured using a photonic multichannel analyzer (PMA-12, Hamamatsu Photonics, Shizuoka, Japan) and monochromatic light from the excitation unit of a fluorimeter (FP-8300, JASCO) as the excitation source. Temperature-dependent measurements were achieved by using a cryostat (Optistat DN-V, Oxford Instruments, Abingdon-on-Thames, UK). The emission yield, including $\Phi_f(T)$ and $\Phi_p(T)$, was measured by the method described in the Supporting Information of a previous report by using an absolute luminescence quantum yield measurement system (C9920-02G, Hamamatsu Photonics) (see section S4 in this article).[11] $\Phi_{isc}(RT)$ in benzene was determined by using the

previously reported method with a subnanosecond transient absorption spectrophotometer (picoTAS, Unisoku, Osaka, Japan) and a 355 nm Q-switched microchip laser (PNV-M02510-1×X0, Teem Photonics, Meylan, France) (see section S2 in this article).

High-Resolution Microscopy Measurements

An inverted optical microscope (Olympus, IX73, Japan) with an oil immersion objective lens (Olympus, UPlan FLN ×100/1.3 NA, oil) was used to achieve high-resolution excitation through a photomask. A laser at 355 nm (PNV-M02510-1×0, Teem Photonics, France) and a laser diode with a wavelength of 445 nm (TC20-4450-4.5, Neoark, Tokyo, Japan) were used as excitation. The emission images were collected using an electron multiplying (EM) CCD camera (iXon Ultra/life 897, Andor Technology, UK). A dichroic mirror (FF470-Di01, Semrock, USA) and a long-pass filter (LP02-473RU, Semrock, USA) were used to excite the sample and collect only the sample emission. For the conditions of the CCD and amplifier, appropriate values of gain and setting temperature were selected depending on the purpose. The excitation power was measured using a photodiode power sensor (S130VC, Thorlabs, Germany). All measurements were performed in air at RT.

Calculations

S_0 and T_1 geometries were calculated by using Gaussian09 based on density functional theory (DFT), and the S_1 geometry was determined by using Gaussian09 based on time-dependent DFT. The B3LYP functional and 6-31G(d) basis sets were used to calculate the molecular orbitals and oscillator strength related to the S_1–S_0 transition at the S_1 geometry. To calculate $\sum_p |\partial\langle T_1|\hat{H}_{SO}|S_0\rangle/\partial Q_p|^2 P(RT)$, vibrations at the T_1 geometry were calculated using Gaussian09 with the B3LYP functional and 6-31G(d) basis sets to determine Q_p. $\langle S_0|\hat{H}_{SO}|T_1\rangle$ that depends on the Q_p from $Q_p = -1.0$ to $Q_p = +1.0$ was calculated by using the Amsterdam Density Functional 2017 package. The parameter $\langle S_0|\hat{H}_{SO}|T_1\rangle$ was treated as a perturbation based on scalar relativistic orbitals with the PBE0 functional and TZP basis sets. Scalar relativistic–time dependent DFT calculations included 1 singlet + 1 triplet excitations, which were used as a basis for the perturbative expansions in the calculations. Detailed procedures have been reported in the literature,[24] and the same procedure and functional and basis sets were used to determine $\sum_p |\partial\langle T_1|\hat{H}_{SO}|S_0\rangle/\partial Q_p|^2 P(RT)$. The T_1 geometry was used to analyze the relationship between k_p and MOs that relate the T_1–S_0 transition (see section S5). A detailed procedure has been reported in the literature,[12,24,39] and the same procedure and functional and basis sets were used to analyze k_p.

ASSOCIATED CONTENT

Supporting Information

The Supporting Information is available free of charge at https://pubs.acs.org/doi/10.1021/jacsau.1c00132.

> NMR and mass spectra of chromophores, supporting optical spectra, data to determine $\Phi_{isc}(RT)$, supporting molecular orbitals and calculation data (PDF)
>
> Video of pRTP emission from **2** under room light (AVI)
>
> Video of pRTP emission from **4** under room light (AVI)
>
> Video of pRTP emission from **3D** under room light (AVI)

AUTHOR INFORMATION

Corresponding Author

Shuzo Hirata − *Department of Engineering Science, The University of Electro-Communications, Chofu, Tokyo 182-8585, Japan;* orcid.org/0000-0003-2591-7678; Email: shuzohirata@uec.ac.jp

Authors

Indranil Bhattacharjee − *Department of Engineering Science, The University of Electro-Communications, Chofu, Tokyo 182-8585, Japan*

Kikuya Hayashi − *Department of Engineering Science, The University of Electro-Communications, Chofu, Tokyo 182-8585, Japan*

Complete contact information is available at:
https://pubs.acs.org/10.1021/jacsau.1c00132

Notes

The authors declare no competing financial interest.

ACKNOWLEDGMENTS

REFERENCES

(1) Reineke, S.; Lindner, F.; Schwartz, G.; Seidler, N.; Walzer, K.; Lüssem, B.; Leo, K. White Organic Light-Emitting Diodes with Fluorescent Tube Efficiency. *Nature* **2009**, *459*, 234−238.

(2) D'Andrade, B. W.; Forrest, S. R. White Organic Light-Emitting Devices for Solid-State Lighting. *Adv. Mater.* **2004**, *16*, 1585−1595.

(3) Sasabe, H.; Kido, J. Development of High Performance OLEDs for General Lighting. *J. Mater. Chem. C* **2013**, *1*, 1699−1707.

(4) Baldo, M. A.; O'Brien, D. F.; You, Y.; Shoustikov, A.; Sibley, S.; Thompson, M. E.; Forrest, S. R. Highly Efficient Phosphorescent Emission from Organic Electroluminescent Devices. *Nature* **1998**, *395*, 151−154.

(5) Adachi, C.; Baldo, M. A.; Thompson, M. E.; Forrest, S. R. Nearly 100% Internal Phosphorescence Efficiency in an Organic Light Emitting Device. *J. Appl. Phys.* **2001**, *90*, 5048−5051.

(6) Lee, J.; Chen, H. F.; Batagoda, T.; Coburn, C.; Djurovich, P. I.; Thompson, M. E.; Forrest, S. R. Deep Blue Phosphorescent Organic Light-Emitting Diodes with Very High Brightness and Efficiency. *Nat. Mater.* **2016**, *15*, 92−98.

(7) Park, H. Y.; Maheshwaran, A.; Moon, C. K.; Lee, H.; Reddy, S. S.; Sree, V. G.; Yoon, J.; Kim, J. W.; Kwon, J. H.; Kim, J. J.; Jin, S. H. External Quantum Efficiency Exceeding 24% with CIE$_y$ Value of 0.08 using a Novel Carbene-Based Iridium Complex in Deep-Blue Phosphorescent Organic Light-Emitting Diodes. *Adv. Mater.* **2020**, *32*, 2002120.

(8) Zhen, X.; Tao, Y.; An, Z.; Chen, P.; Xu, C.; Chen, R.; Huang, W.; Pu, K. Ultralong Phosphorescence of Water-Soluble Organic Nanoparticles for in vivo Afterglow Imaging. *Adv. Mater.* **2017**, *29*, 1606665.

(9) Nicol, A.; Kwok, R. T.; Chen, C.; Zhao, W.; Chen, M.; Qu, J.; Tang, B. Z. Ultrafast Delivery of Aggregation-Induced Emission Nanoparticles and Pure Organic Phosphorescent Nanocrystals by Saponin Encapsulation. *J. Am. Chem. Soc.* **2017**, *139*, 14792−14799.

(10) Zhang, G.; Chen, J.; Payne, S. J.; Kooi, S. E.; Demas, J. N.; Fraser, C. L. Multi-Emissive Difluoroboron Dibenzoylmethane Polylactide Exhibiting Intense Fluorescence and Oxygen-Sensitive Room-Temperature Phosphorescence. *J. Am. Chem. Soc.* **2007**, *129*, 8942−8943.

(11) Hirata, S.; Totani, K.; Zhang, J.; Yamashita, T.; Kaji, H.; Marder, S. R.; Watanabe, T.; Adachi, C. Efficient Persistent Room Temperature Phosphorescence in Organic Amorphous Materials Under Ambient Conditions. *Adv. Funct. Mater.* **2013**, *23*, 3386−3397.

(12) Bhattacharjee, I.; Hirata, S. Highly Efficient Persistent Room-Temperature Phosphorescence from Heavy Atom-Free Molecules Triggered by Hidden Long Phosphorescent Antenna. *Adv. Mater.* **2020**, *32*, 2001348.

(13) Mathew, A. S.; DeRosa, C. A.; Demas, J. N.; Fraser, C. L. Difluoroboron β-diketonate Materials with Long-Lived Phosphorescence Enable Lifetime Based Oxygen Imaging with a Portable Cost Effective Camera. *Anal. Methods* **2016**, *8*, 3109−3114.

(14) Deng, Y.; Zhao, D.; Chen, X.; Wang, F.; Song, H.; Shen, D. Long Lifetime Pure Organic Phosphorescence Based on Water Soluble Carbon Dots. *Chem. Commun.* **2013**, *49*, 5751−5753.

(15) Long, P.; Feng, Y.; Cao, C.; Li, Y.; Han, J.; Li, S.; Peng, C.; Li, Z.; Feng, W. Self-Protective Room-Temperature Phosphorescence of Fluorine and Nitrogen Codoped Carbon Dots. *Adv. Funct. Mater.* **2018**, *28*, 1800791.

(16) Louis, M.; Thomas, H.; Gmelch, M.; Haft, A.; Fries, F.; Reineke, S. Blue-Light-Absorbing Thin Films Showing Ultralong Room-Temperature Phosphorescence. *Adv. Mater.* **2019**, *31*, 1807887.

(17) Fateminia, S. M. A.; Mao, Z.; Xu, S.; Yang, Z.; Chi, Z.; Liu, B. Organic Nanocrystals with Bright Red Persistent Room-Temperature Phosphorescence for Biological Applications. *Angew. Chem., Int. Ed.* **2017**, *56*, 12160−12164.

(18) Yang, J.; Zhen, X.; Wang, B.; Gao, X.; Ren, Z.; Wang, J.; Xie, Y.; Li, J.; Peng, Q.; Pu, K.; Li, Z. The Influence of the Molecular Packing on the Room Temperature Phosphorescence of Purely Organic Luminogens. *Nat. Commun.* **2018**, *9*, 840.

(19) Abdukayum, A.; Chen, J. T.; Zhao, Q.; Yan, X. P. Functional Near Infrared-Emitting Cr^{3+}/Pr^{3+} Co-Doped Zinc Gallogermanate Persistent Luminescent Nanoparticles with Superlong Afterglow for in vivo Targeted Bioimaging. *J. Am. Chem. Soc.* **2013**, *135*, 14125−14133.

(20) Sun, S. K.; Wang, H. F.; Yan, X. P. Engineering Persistent Luminescence Nanoparticles for Biological Applications: from Biosensing/Bioimaging to Theranostics. *Acc. Chem. Res.* **2018**, *51*, 1131−1143.

(21) Pan, Z.; Lu, Y. Y.; Liu, F. Sunlight-Activated Long-Persistent Luminescence in the Near-Infrared from Cr^{3+}-Doped Zinc Gallogermanates. *Nat. Mater.* **2012**, *11*, 58−63.

(22) Yan, S.; Liu, F.; Zhang, J.; Wang, X. J.; Liu, Y. Persistent Emission of Narrowband Ultraviolet-B Light upon Blue-Light Illumination. *Phys. Rev. Appl.* **2020**, *13*, 044051.

(23) Hirata, S. Recent Advances in Materials with Room-Temperature Phosphorescence: Photophysics for Triplet Exciton Stabilization. *Adv. Opt. Mater.* **2017**, *5*, 1700116.

(24) Hirata, S.; Bhattacharjee, I. Vibrational Radiationless Transition from Triplet States of Chromophores at Room Temperature. *J. Phys. Chem. A* **2021**, *125*, 885−894.

(25) Kuila, S.; George, S. J. Phosphorescence Energy Transfer: Ambient Afterglow Fluorescence from Water-Processable and Purely Organic Dyes via Delayed Sensitization. *Angew. Chem., Int. Ed.* **2020**, *59*, 9393−9397.

(26) Zhao, W.; Cheung, T. S.; Jiang, N.; Huang, W.; Lam, J. W.; Zhang, X.; He, Z.; Tang, B. Z. Boosting the Efficiency of Organic Persistent Room-Temperature Phosphorescence by Intramolecular Triplet-Triplet Energy Transfer. *Nat. Commun.* **2019**, *10*, 1595.

(27) Demangeat, C.; Dou, Y.; Hu, B.; Bretonnière, Y.; Andraud, C.; D'Aléo, A.; Wu, J. W.; Kim, E.; Le Bahers, T.; Attias, A. J. σ-Conjugation and H-Bond-Directed Supramolecular Self-Assembly: Key Features for Efficient Long-Lived Room Temperature Phosphorescent Organic Molecular Crystals. *Angew. Chem.* **2021**, *133*, 2476−2484.

(28) Gu, L.; Wu, H.; Ma, H.; Ye, W.; Jia, W.; Wang, H.; Chen, H.; Zhang, N.; Wang, D.; Qian, C.; et al. Color-Tunable Ultralong Organic Room Temperature Phosphorescence from a Multicomponent Copolymer. *Nat. Commun.* **2020**, *11*, 944.

(29) Bian, L.; Shi, H.; Wang, X.; Ling, K.; Ma, H.; Li, M.; Cheng, Z.; Ma, C.; Cai, S.; Wu, Q.; et al. Simultaneously Enhancing Efficiency and Lifetime of Ultralong Organic Phosphorescence Materials by Molecular Self-Assembly. *J. Am. Chem. Soc.* **2018**, *140*, 10734−10739.

(30) Zhao, W.; He, Z.; Lam, J. W.; Peng, Q.; Ma, H.; Shuai, Z.; Bai, G.; Hao, J.; Tang, B. Z. Rational Molecular Design for Achieving Persistent and Efficient Pure Organic Room-Temperature Phosphorescence. *Chem.* **2016**, *1*, 592−602.

(31) Kamatsuki, T.; Bhattacharjee, I.; Hirata, S. The Substituent-Induced Symmetry-Forbidden Electronic Transition Allows Significant Optical Limiting under Weak Sky-Blue Irradiance. *J. Phys. Chem. Lett.* **2020**, *11*, 8675−8681.

(32) Huang, R.; Avó, J.; Northey, T.; Chaning-Pearce, E.; dos Santos, P. L.; Ward, J. S.; Data, P.; Etherington, M. K.; Fox, M. A.; Penfold, T. J.; et al. The Contributions of Molecular Vibrations and Higher Triplet Levels to the Intersystem Crossing Mechanism in Metal-Free Organic Emitters. *J. Mater. Chem. C* **2017**, *5*, 6269−6280.

(33) Burrows, H.; Fernandes, M.; de Melo, J.; Monkman, A.; Navaratnam, S. Characterization of the Triplet State of Tris(8-hydroxyquinoline)aluminium(III) in Benzene Solution. *J. Am. Chem. Soc.* **2003**, *125*, 15310−15311.

(34) Gu, L.; Shi, H.; Bian, L.; Gu, M.; Ling, K.; Wang, X.; Ma, H.; Cai, S.; Ning, W.; Fu, L.; et al. Colour-Tunable Ultra-Long Organic Phosphorescence of a Single-Component Molecular Crystal. *Nat. Photonics* **2019**, *13*, 406−411.

(35) Robinson, G. W.; Frosch, R. P. Electronic Excitation Transfer and Relaxation. *J. Chem. Phys.* **1963**, *38*, 1187−1203.

(36) Schlag, E. W.; Schneider, S.; Fischer, S. F. Lifetimes in Excited States. *Annu. Rev. Phys. Chem.* **1971**, *22*, 465−526.

(37) Kropp, J. L.; Dawson, W. R. Radiationless Deactivation of Triplet Coronene in Plastics. *J. Phys. Chem.* **1967**, *71*, 4499−4506.

(38) Kwon, M. S.; Yu, Y.; Coburn, C.; Phillips, A. W.; Chung, K.; Shanker, A.; Jung, J.; Kim, G.; Pipe, K.; Forrest, S. R.; et al. Suppressing Molecular Motions for Enhanced Room-Temperature Phosphorescence of Metal-Free Organic Materials. *Nat. Commun.* **2015**, *6*, 8947.

(39) Hirata, S. Intrinsic Analysis of Radiative and Room-Temperature Nonradiative Processes Based on Triplet State Intramolecular Vibrations of Heavy Atom-Free Conjugated Molecules Toward Efficient Persistent Room-Temperature Phosphorescence. *J. Phys. Chem. Lett.* **2018**, *9*, 4251−4259.

(40) Metz, F.; Friedrich, S.; Hohlneicher, G. What is the Mechanism for the Nonradiative Decay of the Lowest Triplet State of Aromatic Hydrocarbons? *Chem. Phys. Lett.* **1972**, *16*, 353−358.

(41) Siebrand, W. Mechanism of Radiationless Triplet Decay in Aromatic Hydrocarbons and the Magnitude of the Franck—Condon Factors. *J. Chem. Phys.* **1966**, *44*, 4055−4057.

(42) Siebrand, W.; Williams, D. F. Isotope Rule for Radiationless Transitions with an Application to Triplet Decay in Aromatic Hydrocarbons. *J. Chem. Phys.* **1967**, *46*, 403−404.

(43) Hirata, S.; Totani, K.; Yamashita, T.; Adachi, C.; Vacha, M. Large Reverse Saturable Absorption under Weak Continuous Incoherent Light. *Nat. Mater.* **2014**, *13*, 938−946.

(44) Hirata, S.; Vacha, M. Large Transmittance Change Induced by Exciton Accumulation under Weak Continuous Photoexcitation. *Adv. Opt. Mater.* **2016**, *4*, 297−305.

(45) Zhou, B.; Yan, D. Simultaneous Long-Persistent Blue Luminescence and High Quantum Yield within 2D Organic−Metal Halide Perovskite Micro/Nanosheets. *Angew. Chem., Int. Ed.* **2019**, *58*, 15128−15135.